Influence of human epidermal thickness on penetration depth of detected photons in spatially-resolved diffuse reflectance spectroscopy: a numerical study

Victor Colas, Christian Daul, Khairallah Gregoire, Marine Amouroux, Walter Blondel

Influence of human epidermal thickness on penetration depth of detected photons in spatially-resolved diffuse reflectance spectroscopy: a numerical study

Colas, Victor, Daul, Christian, Khairallah, Gregoire, Amouroux, Marine, Blondel, Walter

Victor Colas, Christian Daul, Gregoire Khairallah, Marine Amouroux, Walter Blondel, "Influence of human epidermal thickness on penetration depth of detected photons in spatially-resolved diffuse reflectance spectroscopy: a numerical study," Proc. SPIE 11640, Optical Interactions with Tissue and Cells XXXII, 116400H (5 March 2021); doi: 10.1117/12.2578203

SPIE.

Event: SPIE BiOS, 2021, Online Only

Influence of human epidermal thickness on penetration depth of detected photons in spatially-resolved diffuse reflectance spectroscopy: a numerical study

Victor Colas*[1], Christian Daul[1], Grégoire Khairallah[1,2], Marine Amouroux[1], and Walter Blondel[1]

[1]Université de Lorraine, CNRS, CRAN, F-54000 Nancy, France
[2]Metz-Thionville Regional Hospital, Department of plastic, aesthetic and reconstructive surgery, Ars-Laquenexy, 57530, France

ABSTRACT

In the context of cutaneous carcinoma *in vivo* diagnosis, Diffuse Relectance (DR) acquired using Spatially Resolved (SR) optical biopsy, can be analysed to discard healthy from pathological areas. Indeed, carcinogenesis induces local morphological and metabolic changes affecting the skin optical answer to white light excitation. The present contribution aims at studying the epidermis thickness impact on the path and propagation depth distribution of DR photons in skin in the perspective of analyzing how these photons contribute to the corresponding acquired spectra carrying local physiological information from the visited layers. Modified *CudaMCML*-based simulations were performed on a five-layer human skin optical model using (i) wavelength-resolved scattering and absorption properties and (ii) the geometrical configuration of a multi-optical fiber probe implemented on a SR-DR spectroscopic device currently used in clinics. Through maps of scattering events and histograms of maximum probed depth, we provide numerical evidences linking the characteristic penetration depth of the detected photons to their wavelengths and four source-sensor distances for thin, intermediate and wide skin thicknesses model. The study provides qualitative and quantitative tools that can be useful during the design of an optical SR-DR spectroscopy biopsy device.

Keywords: Skin optics, spatially-resolved diffuse reflectance spectroscopy, photon depth penetration, skin layer probed, diagnosis of cutaneous carcinoma, modelling study, Monte Carlo simulation

1. INTRODUCTION

Diffuse Reflectance Spectroscopy (DRS) applied to biological tissues is a widely used, non-destructive optical characterization technique, consisting in measuring back-reflected intensity spectra resulting from light-matter interactions, from which the optical and structural properties of the probed medium can then be extracted and analyzed. The source fiber (SF) emitting UV-Visible-NIR light at one tissue point can be separated from one or several detection fibers (DF) located at different source-detector (SD) distances. We then talk about spatially-resolved (SR) DRS. Depending on the SD distances implemented, it allows to probe different depths in the tissue. This added value makes sense when the environments are inhomogeneous in depth, which is particularly the case of human skin composed of several distinct layers. Due to its sensitivity to metabolic and structural changes in tissues and its clinical applicability, SR-DRS is very well suited to *in vivo* biomedical diagnostics. That is why the literature offers a large number of applications to characterize cutaneous pathological states from SR-DR spectra measurements. Hence, several studies on the diagnosis of skin cancers were carried out, including melanoma[1–3] and carcinoma,[4,5] and more generally on skin layer optical properties characterization.[6,7]

In this context of skin optical biopsy, a point spectroscopy device exploiting light-induced intrinsic fluorescence and DR spectroscopy modalities was designed and patented by our team (*SpectroLive*[8]). This device is currently being used in a clinical study whose purpose is to assist the surgeon establishing surgical margins during skin carcinoma resection.[9] The estimation of diagnostically relevant optical parameters from *in vivo* SR-DR spectra,

victor.colas@univ-lorraine.fr, phone: +33 (0)6 65 41 60 46

Optical Interactions with Tissue and Cells XXXII, edited by Bennett L. Ibey, Norbert Linz, Proc. of SPIE
Vol. 11640, 116400H · © 2021 SPIE · CCC code: 1605-7422/21/$21 · doi: 10.1117/12.2578203

and especially their evolution around the lesion can be linked to the tissue pathological state. The skin layer optical parameters will be obtained by solving the inverse problem,[10,11] where simulated spectra result from an adaptation of *CudaMCML* code developed by Alerstam *et al.*[12] to fit our clinical device configuration features. In order to learn more about the behavior of photons detected in depth, and thus allow for a better interpretation of the simulated and measured DR signals, numerical tools was implemented on our simulation. The present contribution deals with the design and exploitation of this tools, *i.e.* scattering trajectory maps and histograms of maximum probed depth for the photons detected at different SD distances. This information was determined for realistic multi-layered skin model in accordance with the geometrical configuration of the clinical device. The in-depth characterization was led for three media of thin, intermediate and large epidermis thickness value to consider the body location dependency.

2. MATERIALS AND METHODS

2.1 Geometrical and spectral description of the SR-DRS probe

The geometrical and optical features of source and detector fibers implemented in our SR-DR spectroscopy simulations were based on the technical characteristics of the aforementioned *SpectroLive* device. The multiple fiber optic probe of the clinical device consists of a central SF of radius $r_{SF} = 300\ \mu m$ and numerical aperture $NA_{SF} = 0.22$ delivering broadband [365-765] nm white light illumination to the tissue in contact, and of 24 detection fibers (DF) of radius $r_{DF} = 200\ \mu m$ and $NA_{DF} = 0.22$ each, equally distributed on 4 concentric circles corresponding to the 4 SD center-to-center distances D_n ($n \in \{1, ..., 4\}$) from 400 to 1000 μm by 200 μm step. The photons reaching one of the 6 collection fibers of the D_n distance are colligated to constitute the diffuse reflectance signal $DR_{D_n}(\lambda)$. A schematic representation of the acquisition geometry is shown in Fig. 1, while the numerical values of the different parameters used are summarized in the Table 1.

$[\lambda_{min}, \lambda_{max}]$ (nm)	D_n (μm)	$NA_{SF/DF}$	r_{SF} (μm)	r_{DF} (μm)
[365,765]	400,600,800,1000	0.22	300	100

Table 1. Values of the geometrical and spectral source-detector features for the SR-DRS simulation.

2.2 Skin five-layered model description

2.2.1 Thicknesses of epidermis layers to mimic several body locations

The skin mimicking numerical model was designed following a five planar multi-layered medium, representing (from superficial to deepest layers): the stratum corneum (1-SC), the living epidermis (2-LE), the papillary dermis (3-PD), the reticular dermis (4-RD) and the subcutaneous fat (5-SF). The total thickness was fixed to $z^{tot} = 6120\ \mu m$, while the total radius of the simulation medium was set to $r^{tot} = 3000\ \mu m$. Considering the order of magnitude of skin optical properties, and the position of the the farthest collecting fiber ($D_4 = 1000\ \mu m$), edge effects (*i.e.* photons that would leave the medium by the lower borders or the sides) were negligible. This was verified numerically with absorption maps.

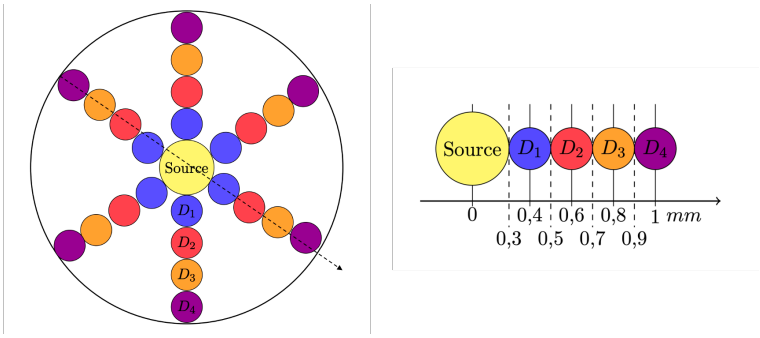

Figure 1. Geometrical disposition of the Source Fiber (SF) and Detection Fiber (DF) of the *SpectroLive* probe.

The epidermis, made of SC and LE, is the layer for which the thickness may significantly vary according to age, gender, and especially body location.[13–15] Thus, different combinations of SC and LE thickness values (respectively z^1 and z^2) were defined to implement skin models in our simulation to represent the acquisition of DR spectra at different cutaneous sites. Others layer thicknesses were fixed at $z^3 = 200\ \mu m$ for PD and $z^4 = 1800\ \mu m$ for RD, while the SF thickness z^5 were adjusted to keep the total thickness z^{tot} of medium constant. We considered the range of values of SC and LE thicknesses as well as their approximate ratio ($\sim 1/4$) reported for sun-exposed skin sites only (head including face, scalp, ear, cheek, shoulders, back, arms, back of hand and legs) that are $[10-30]\mu m$ and $[60-120]\mu m$ for SC and LE layers respectively. The numerical values associated with the elaboration of these 3 simulation media configurations are summarized in Table 2.

Skin Thickness	SC thickness z^1 (μm)	LE thickness z^2 (μm)
Smallest thicknesses	10	60
Mean thicknesses	20	90
Highest thicknesses	30	120

Table 2. Values of the SC and LE layer thicknesses implemented in our skin model to simulate 3 different skin body sites.

2.2.2 Skin layers optical properties

Absorption properties: The absorption coefficients $\mu_a^k(\lambda)$ were defined for each layer $k \in \{1..5\}$ taking into account five main chromophores of human skin *i.e.* blood, water, melanin, lipids and β-caroten, as well as their relative concentrations. The mixed contribution into the layer k of the latter compounds was expressed as:[16]

$$\mu_a^k(\lambda) = \sum_i f_{v,i}^k \mu_{a,i}^k(\lambda) + \mu_{a,base}(\lambda) \tag{1}$$

Where $\mu_{a,i}^k(\lambda)$ is the absorption coefficient (cm^{-1}) of chromophore $i \in \{blood, water, mel, lipids, \beta - caroten\}$ in layer k, $f_{v,i}^k$ its volume fraction (dimensionless) in the mixture and $\mu_{a,base}(\lambda)$ a residual absorption baseline contribution introduced in Meglinski and Matcher article.[17] Expressions of $\mu_{a,base}(\lambda)$, as well as details to obtain $\mu_{a,i}^k(\lambda)$ for each layer, and finally the values of $f_{v,i}^k$ set in simulation are available in a previous contribution using the same optical medium description.[18] Considering our targeted clinical application of interest, *i.e.* the skin carcinoma diagnosis, it was chosen to consider a melanosome volume fraction in LE $f_{v,mel}^2 = 0.01$ corresponding to phototype I (very fair skin), which is much more prone to the development of skin cancer. The resulting absorption spectra are shown in Fig. 2.

Scattering properties: Skin scattering coefficients $\mu_s^k(\lambda)$ in the various layers of our model were obtained from equation (2) given by Aravind Krishnaswamy *et al.*[19] featuring two contributions: a blood scattering component and a bloodless "base" scattering component.

$$\mu_s^k(\lambda) = (1 - f_{v,blood}^k)\mu_{s,base}^k(\lambda) + f_{v,blood}^k C_{blood}^k(\lambda)\mu_{s,blood}(\lambda) \tag{2}$$

Where $\mu_{s,base}^k(\lambda)$ is the layer-dependent bloodless scattering coefficient, $\mu_{s,blood}(\lambda)$ the scattering coefficient of pure blood from OMLC database,[20] $f_{v,blood}^k$ the blood volume fraction in layer k and finally $C_{blood}^k(\lambda)$ a correction factor dependent on the mean vessels diameter of the layer and the illumination conditions. Once again, values set in the simulation for the aforementioned parameters are fully described in our latter contribution.[18] The resulting absorption spectra also appear in in Fig. 2.

Other optical parameters: Both the anisotropy factor g and the refractive index n were considered as wavelength-independent. The first one value was set to $g = 0.9$ whatever the layer while the second one value was set to $n^1 = 1.55$, $n^2 = 1.44$, $n^3 = 1.39$, $n^4 = 1.41$, $n^5 = 1.44$, in every of the 5 layers respectively.

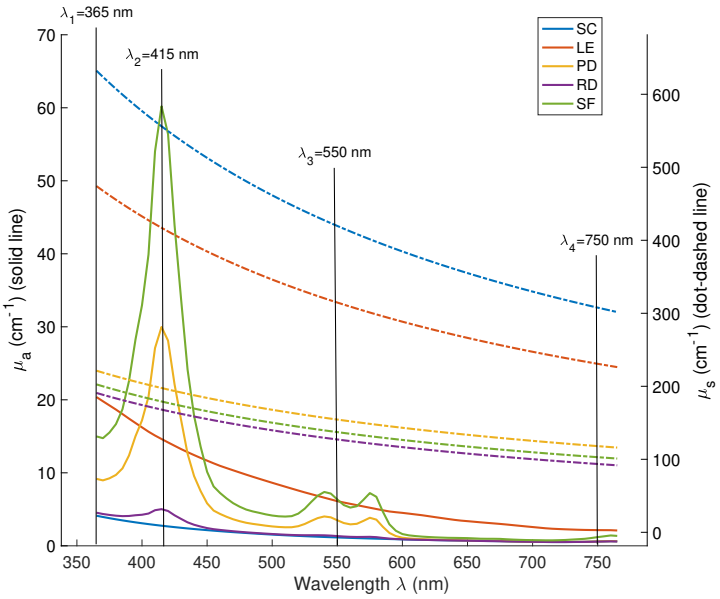

Figure 2. Absorption (μ_a solid line) and scattering (μ_s dot-dashed line) coefficients of each layer (SC, LE, PD, RD and SF in blue, red orange, violet and green respectively) of the designed numerical medium. Black vertical lines represents the 4 wavelengths of interest for which the trajectory maps and depths probed histograms are illustrated in section 3.1.

2.3 Simulation configuration, method and tools

2.3.1 Simulation configuration

The simulation algorithm developed was based on the *CudaMCML* code from Alerstam *et al.*[12] It was modified to mimic a real acquisition of *SpectroLive* device features.[21] Multi-thread calculations were performed to simulate the photon propagation on a *DELL T630* device using the *Intel Xeon E5-2683v4 2.1 GHz, AVX* CPU and the *GEFORCE GTX 1080 Ti* GPU card cluster available within the High Performance Computing resources center "Explor" at the University of Lorraine. The sending of 81×10^8 photons for the reacquired 81 wavelengths between 365 and 765 nm (corresponding to a spectral resolution of 5 nm) were spread in 8960 threads in 28 blocks (*i.e.* 320 threads/block), for an approximate calculation time of 10^3 s. Finally, the spatial resolutions according to radial distance and depth were respectively set to $dz = 5\ \mu m$ and $dr = 10\ \mu m$.

2.3.2 Photon propagation algorithm and detection conditions

To fit our *SpectroLive* clinical device, geometric detection constraints were added to the original code, including the DF positions and their numerical aperture (*cf.* Table 1). Details about photons propagation algorithm and detection conditions are exposed in our previous work.[18] These modifications allow for the acquisition of simulated SR-DR spectra $DR_{D_n}(\lambda)$ which unit is the photons ratio, comprised of photons having reached the DF located at the SD distance D_n.

2.3.3 Trajectory maps and maximum probed depth histograms

Trajectory maps and depth probed histograms were determined to enable qualitative and quantitative analysis of the detected photon penetration depths and propagation paths, especially to link the skin layer probed to the couple (λ, D_n). The algorithms allowing to obtain the latter data sets were presented in our previous contribution.[18] Each can be applied at a given source to detector distance, and at a given wavelength.

Trajectory maps are a 2D representation of the 3D medium matrix described in the *CudaMCML* algorithm, in which the source appears in the top left corner, the vertical axis represents the medium's depth and the horizontal axis the medium's radial distance to source. The z-axis (color chart intensity displayed in log scale) has to be interpreted as a relative volume density. Indeed, for a given pixel (i, j) corresponding to a (z_i, r_j)

position in the 2D matrix medium, the intensity is the sum of all detected photons weights that was subjected to a scattering event on this position, divided by the voxel volume and the total number of scattering events for the considered couple (λ, D_n). Thus, the resulting map reflects the distribution (in the sense of spreading) of scattering events between the SF and DF.

For the maximum probed depth histograms, it consists in storing the lowest point of the optical path z_{max} between SF and DF for each detected photon before grouping and then counting those that have reached the same depth (in an interval of $dz = 5\mu m$). We thus obtain an histogram in which the abscissa is the maximal probed depth z_{max} and the ordinate is the occurrence in photons count. To better represent the depth distribution and being able to compare those histograms for different wavelengths and SD distances, it was chosen to normalize this output by dividing the occurrence value by the total number of collected photons for the couple (λ, D_n). The $y - axis$ finally becomes a relative photons count occurrence that appears in percentage in paragraph 3.1.2.

3. RESULTS AND DISCUSSION

3.1 Presentation of the mean thicknesses medium results

Results presented in this sub-section are associated to mean thicknesses medium presented in Table 2. Study on skin epidermal thickness variation is available in sub-section 3.2. For the sake of brevity, the DR spectra associated with this medium configuration are not represented in this sub-section but appear in Fig. 8 (dashed line) with the other spectra associated to thin and thick configuartions.

3.1.1 Wavelength and SD distance dependencies on trajectory maps

The optical device offers the possibility to play on 2 parameters, namely the value of the SD distance and the wavelength, to access different deep layers of the skin. Thus, Fig. 3 shows the probed volume for $\lambda_2 = 415\ nm$ (left) and $\lambda_3 = 550\ nm$ (right) for the same SD distance $D_4 = 1000\ \mu m$. By looking at the optical properties for these wavelengths (see black vertical lines in Fig. 2), we can explain that the detected photons come from deeper trajectories because of the greater optical transparency of the medium for the second wavelength, *i.e.* $\mu_a(\lambda_2) + \mu_a(\lambda_2) > \mu_a(\lambda_3) + \mu_a(\lambda_3)$.

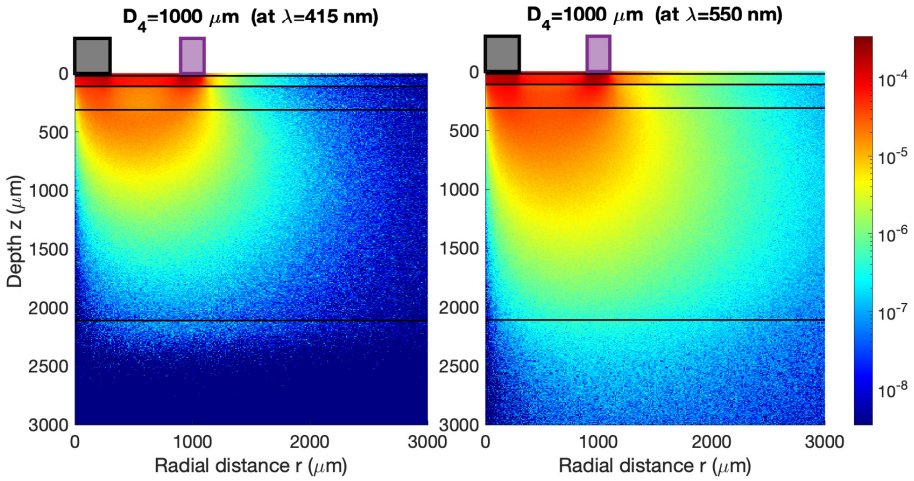

Figure 3. Trajectory maps at $\lambda_2 = 415\ nm$ and $\lambda_3 = 550\ nm$ for the 4^{th} SD ($D_4 = 1000\ \mu m$) distance simulated for the 5-layer skin model with intermediate thicknesses of SC and LE layers. A zoom on a 3000 $\mu m \times 3000\ \mu m$ top-left square area was performed for a better visualization of the photons trajectories. Black and purple squares respectively represent the SF and DF.

It is also possible to adjust the SD distance to access different skin tissue depths. Fig. 4 shows the evolution of the trajectory maps for $\lambda_1 = 365\ nm$ and the 4 SD distances. We can observe the typical path between SF and DF called "Banana shape",[6,22,23] and the expected behavior when D_n increases: DR spectra are composed of photons that have plunged deeper into the medium.

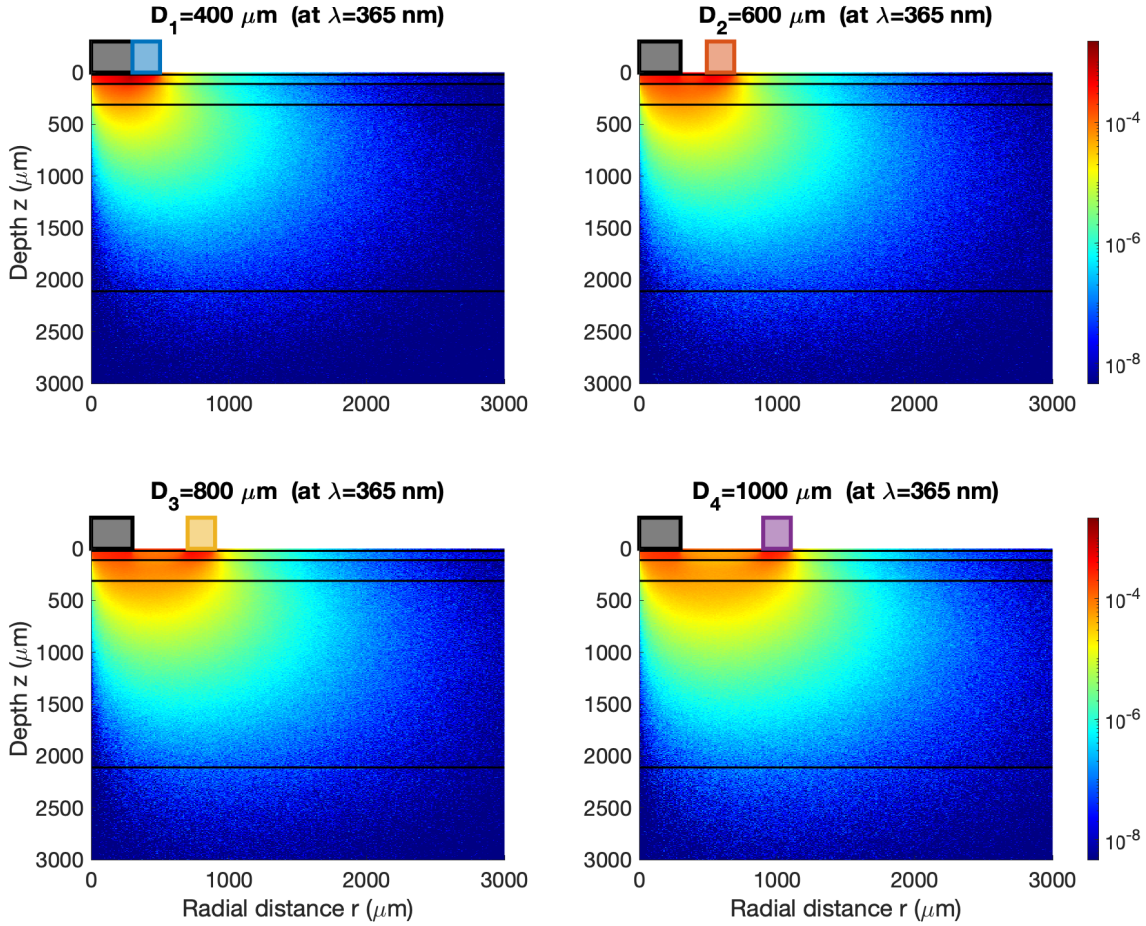

Figure 4. Trajectory maps at $\lambda_1 = 365\ nm$ for the 4 SD distances simulated for the 5-layer skin model with intermediate thicknesses of SC and LE layers. A zoom on a 3000 $\mu m \times 3000\ \mu m$ top-left square area was performed for a better visualization of the photons trajectories. Black square represents the SF, while the colored ones stand for the different DF.

3.1.2 Wavelength and SD distance dependencies on maximum probed depth histograms

It is a question of studying more quantitatively the impacts of each of the parameters of the pair (λ, D_n) through the histgograms of maximum depth probed. Fig. 5 illustrates the λ dependency, by providing the histograms for the four wavelengths pinned with black vertical lines in Fig. 2 for D_4 SD distance. We can notice the global offset toward deeper probed depths when λ scans the visible range from near UV to NIR wavelengths, excepted for $\lambda_2 = 415\ nm$ corresponding to hemoglobin absorption peak. The presence of abrupt transitions is also noticeable in the histograms corresponding to refractive index mismatch (*i.e.* reflection) between consecutive layers, represented by a black vertical line. Finally, a box-plot approach was chosen to extract a characteristic probed depth associated to the couple (λ, D_n). Thus, the 3 vertical colored lines for each of the histograms represent from left to right: the 1^{st} quartile (dotted) Z_{q1}, the median (solid line) Z_{med} and the 2^{nd} quartile (dotted) Z_{q2}. The colored area under the histogram, between the two quartiles, then represents 50 % of the total area. In other words, half of the photons contributing to the $DR_{D_n}(\lambda)$ value have reached at most a depth between Z_{q1} and Z_{q2}.

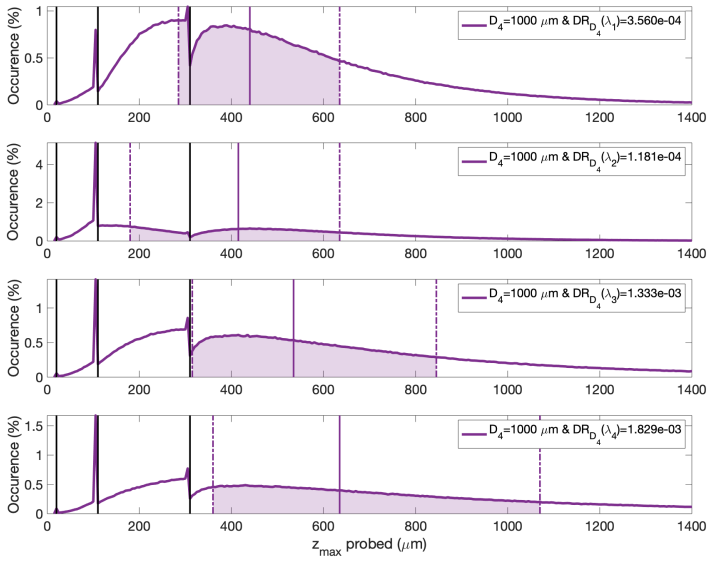

Figure 5. Maximum probed depth histograms at $\lambda_1 = 365\ nm$, $\lambda_2 = 415\ nm$, $\lambda_3 = 550\ nm$ and $\lambda_4 = 750\ nm$ for the 4^{th} SD ($D_4 = 1000\ \mu m$) distance simulated for the 5-layer skin model with intermediate thicknesses of SC and LE layers. SF does not appear because the amount of photons that reach this layer is negligible.

For the impact of SD distance, Fig. 6 displays the histograms at $\lambda_1 = 365\ nm$ for the 4 available detector positions. The graphic conventions are the same as in the previous Fig. 3. We can notice that photons go deeper, as well as the widening of the probed volume (visible here in the form of the inter-quartiles enlargement) for longer SD distances than shorter ones.

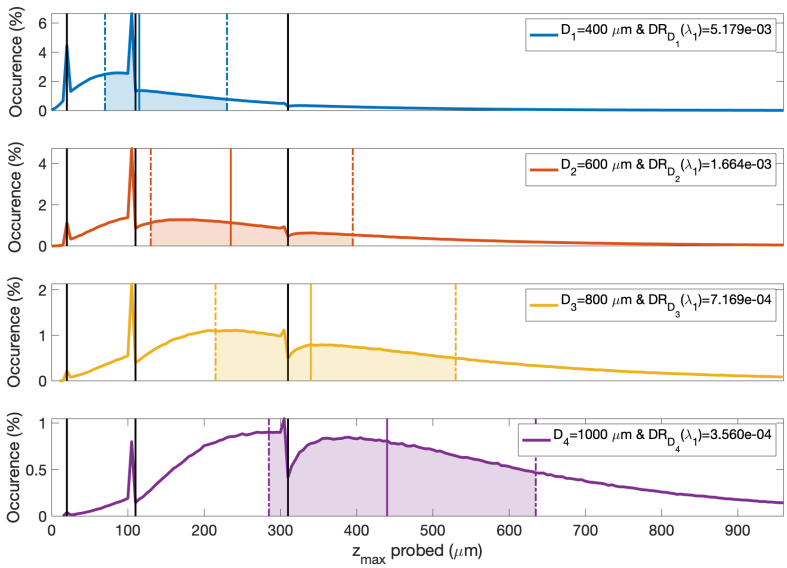

Figure 6. Maximum probed depth histograms at $\lambda_1 = 365\ nm$ for the 4 SD distances simulated for the 5-layer skin model with intermediate thicknesses of SC and LE layers. SF does not appear because the amount of photons that reach this layer is negligible.

Since all these histograms are available for each of D_n, as well as for all the emitted wavelengths, it was chosen to synthesize the spectral penetration behavior of the detected photons by extracting the median and the quartiles for all couples (λ, D_n). The results obtained from these calculations are presented in Fig. 7, with the same graphic conventions. The quasi-linearity of the probed depth can be seen as a function of the two varying parameters excepted in the first hemoglobin absorption peak (415 nm). More importantly, it can be noticed that the spatial resolution and spectral range of the device allow to probe depths covering the interval $[50, 1050]$ μm. Moreover, one can read there, that the photons having contributed to the spectrum $DR_{D_4}(\lambda)$ and verifying $\lambda > 450$ nm have largely visited at most the RD layer. On the other hand, it is visible that the photons of $DR_{D_1}(\lambda)$ satisfying $\lambda < 450$ nm remained globally confined in SC, LE and PD layers. One can also observe that the inter-quartiles range widens when λ increases, and this for all distances D_n. Indeed, the probed volume is very localized for the near UV wavelengths and spreads when it approaches the NIR ones.

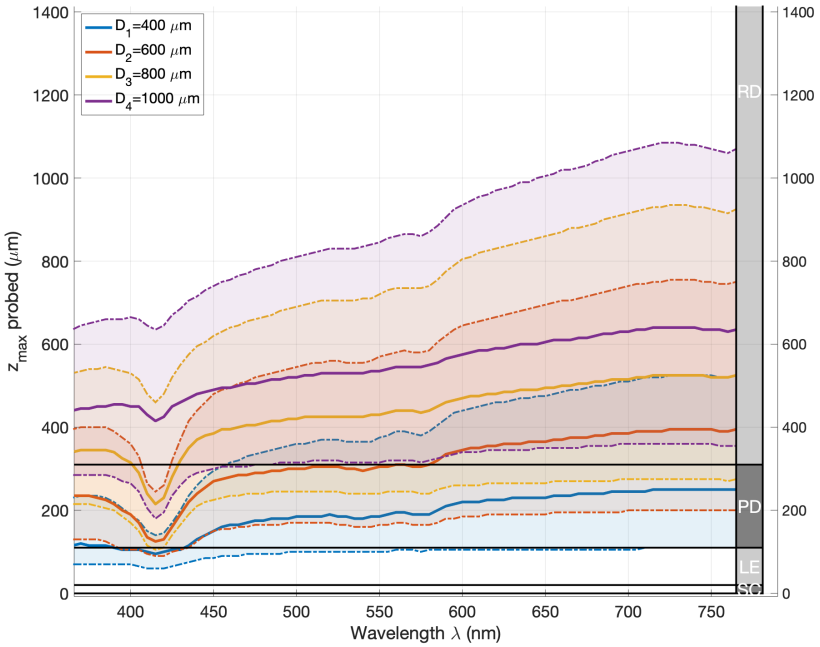

Figure 7. Maximal probed depth values of detected photons in the skin model with intermediate thicknesses of SC and LE layers, as a function of wavelength and SD distances. Solid and dot-dashed lines represent median and quartiles values respectively. The right column and the black horizontal lines illustrate the position of the diopters between the layers.

3.2 DR spectra and evolution of the probed depth for different epidermal thicknesses

Results presented here are associated to epidermis thicknesses value presented in Table 2. It aim to observe the evolution of DR spectra and to analyze it using the in-depth numerical tools created when the thickness of the epidermis varies.

3.2.1 DR spectra for variable epidermal thickness

By looking on the DR spectra available on Fig. 8, it is noteworthy to point that (i) at D_1, the amplitude of the DR spectrum for max thickness epidermis is greater than the one for min thickness epidermis whatever the wavelengths, while (ii) along with longer SD distances, the amplitude of the DR spectra for max thickness epidermis tends to be lower than the one of min thickness epidermis. Let us try to explain this behavior by analyzing the origin of the detected photons (*i.e.* the skin layers they visited) for each of the thin, median and thick media.

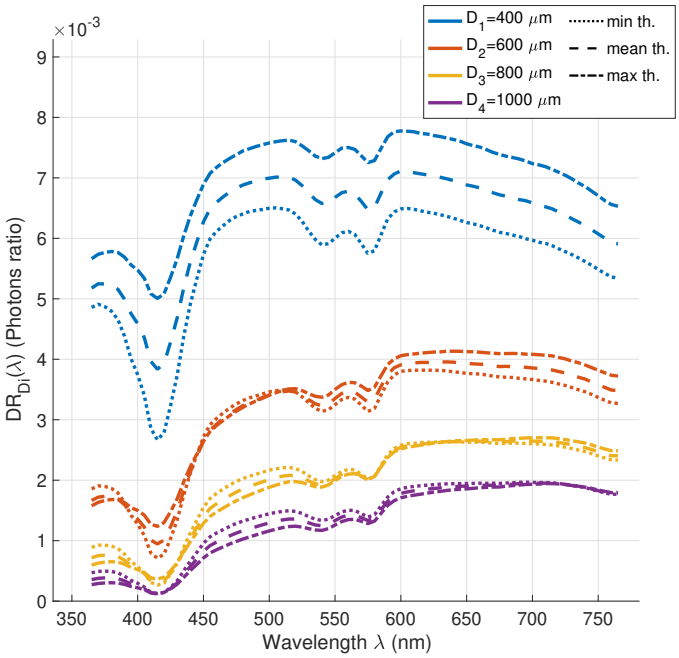

Figure 8. DR spectra for the 3 thin (dotted line), mean (dashed) and thick media (dashed-dot). The distance SD D_n is indicated by the color code, while the line style refers to the medium.

3.2.2 Probed depth for variable epidermal thicknesses

The maximal probed depth values of detected photons for the small, mean and high thicknesses media (see Table 2) is available on Fig. 9. If we observe the probed depth at D_1 for the thickest epidermis model, we notice that most of the photons having contributed to $DR_{D_1}(\lambda)$ remained confined in SC and LE layers. For the thinnest epidermis model, the photons have largely visited the PD layer, and even the RD one especially for the near IR wavelengths. The evolution of the spectra of $DR_{D_1}(\lambda)$ for the different thicknesses may be explained by the high scattering capacity of the SC and LE layers at the origin of a short path length return of many photons to the surface (and thus captured at D_1). If we now consider D_4 the figure of the probed depths shows us that, in general, the increase of the SD distance forces the photons to dive into the depths of the medium: the superficial back-scattering effect is no longer observed. The refinement of the SC and LE layers allows the photons to penetrate deeper into the RD one. The resulting optical path is then more consequent, which could explain a decrease of $DR_{D_4}(\lambda)$ with the thickening of the skin. The photon propagation of the distances D_2 and D_3 would then correspond to a transitional state between these two modes.

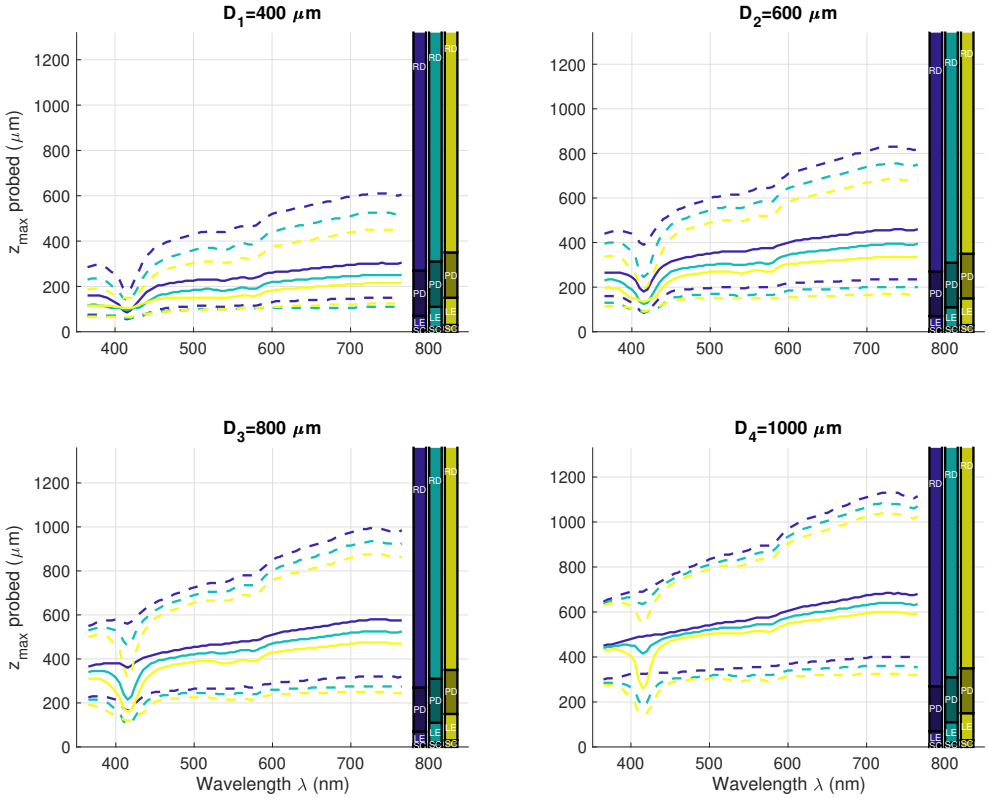

Figure 9. Maximal probed depth values of detected photons in the skin model with minimum (blue), intermediate (green) and maximum (yellow) thicknesses of SC and LE layers, as a function of wavelength and SD distances. Solid and dot-dashed lines represent median and quartiles values respectively. The right column illustrate the position of the diopters between the layers, in every medium configuration (*cf.* Table 2).

4. CONCLUSION

In order to learn more about the behavior of photons detected in depth, and thus allow for a better interpretation of the simulated and measured diffuse reflectance signals, a numerical study was designed. A photon propagation algorithm was adapted to match the measurement of *SpectroLive* instrument, a spatially-resolved diffuse reflectance spectroscopy device used in clinical applications. To do so, a numerical five-layered skin optical model, including realistic absorption and scattering properties from main intrinsic chromophores was defined. The trajectory maps first allowed to visualize the typical path (banana shape) followed by the photons detected at a fixed wavelength and source-detector distance, while the histograms of probed depths and their exploitation allowed us to extract the characteristic depths at which the photons undertake the return path to the collection fiber. We finally analyzed the evolution of DR spectra with the widening or narrowing of the epidermis to mimic the displacement of the probe on several body sites by using the implemented numerical tools.

ACKNOWLEDGMENTS

The authors would like to thank French Région Grand-Est, CNRS and Metz-Thionville Regional Hospital (2016 clinical research Award) in the frame of the SpectroLive project, Contrat de Plan Etat - Région Grand Est 2015-2020 (CPER IT2MP, plateforme IMTI) including the European Regional Development Fund FEDER, the Ligue Contre le Cancer institute, and Lorraine Université d'Excellence (LUE) Doctorate 2019 under the PhD grant R01PJYRX-PHD19-COLA-CRAN (Victor Colas, 2019-2022). High Performance Computing resources were partially provided by the EXPLOR centre hosted by the Université de Lorraine (project 2018AM2IX0877).

REFERENCES

[1] Garcia-Uribe, A., Wang, L. V., Zou, J., Smith, E. B., M.D., M. D., and Prieto, V., "In-vivo characterization of optical properties of pigmented skin lesions including melanoma using oblique incidence diffuse reflectance spectrometry," *Journal of Biomedical Optics* **16**(2), 1 – 3 (2011).

[2] Pires, L., Demidov, V., Vitkin, I. A., Bagnato, V. S., Kurachi, C., and Wilson, B. C., "Optical clearing of melanoma in vivo : characterization by diffuse reflectance spectroscopy and optical coherence tomography," *Journal of Biomedical Optics* **21**, 081210 (2016).

[3] Amouroux, M., Blondel, W., Granel-Brocard, F., Marchal, F., and Guillemin, F., "A preliminary study on skin phantoms to test spatially resolved-Diffuse Reflectance Spectroscopy as a tool to help diagnose cutaneous melanoma: A non-invasive measurement of Breslow index.," *Bio-Medical Materials and Engineering* **18**(4-5), 339–343 (2008).

[4] Khairallah, G., Blondel, W., Rakotomanga, P., Soussen, C., Delconte, A., Plenat, F., Marchal, F., and Amouroux, M., "Impact of standardization of autofluorescence and diffuse reflectance spectra on diagnosis accuracy of optical spectroscopy used for skin carcinomas diagnosis.," in [*In Saratov Fall Meeting SFM'18 International Symposium"Optics and Biophotonics-V*], (2018).

[5] Amouroux, M., Díaz-Ayil, G., and Blondel, W. C. P. M., "Classification of ultraviolet irradiated mouse skin histological stages by bimodal spectroscopy: multiple excitation autofluorescence and diffuse reflectance," *Journal of Biomedical Optics* **14**, 14011– 14 (2009).

[6] Koenig, A., Roig, B., Digabel, J. L., Josse, G., and Dinten, J.-M., "Accessing deep optical properties of skin using diffuse reflectance spectroscopy," in [*Clinical and Biomedical Spectroscopy and Imaging IV*], Brown, J. Q. and Deckert, V., eds., **9537**, 42 – 49, International Society for Optics and Photonics, SPIE (2015).

[7] Naglič, P., Pernuš, F., Likar, B., and Bürmen, M., "Estimation of optical properties by spatially resolved reflectance spectroscopy in the subdiffusive regime," *Journal of Biomedical Optics* **21**(9), 1 – 11 (2016).

[8] Amouroux, M., Blondel, W., and Delconte., A., "Medical device for fibered bimodal optical spectroscopy," (2017). World patent number: WO2017093316 (A1).

[9] Khairallah, G., Amouroux, M., Plénat, F., Rakotomanga, P., Soussen, C., Marchal, F., Delconte, A., Chen, H., and Blondel, W., "Spatially resolved spectroscopy for guiding margin delineation during human skin carcinomas resection: first clinical results on diffuse reflectance and autofluorescence spectra and in vivo skin optical properties," in [*Biophotonics: Photonic Solutions for Better Health Care VI*], Popp, J., Tuchin, V. V., and Pavone, F. S., eds., **10685**, 200 – 206, International Society for Optics and Photonics, SPIE (2018).

[10] Cen, H., Lu, R., and Dolan, K., "Optimization of inverse algorithm for estimating the optical properties of biological materials using spatially-resolved diffuse reflectance," *Inverse Problems in Science and Engineering* **18**(6), 853–872 (2010).

[11] Palmer, G. M. and Ramanujam, N., "Monte carlo-based inverse model for calculating tissue optical properties. part i: Theory and validation on synthetic phantoms," *Appl. Opt.* **45**, 1062–1071 (Feb 2006).

[12] Erik Alerstam, Tomas Svensson, S. A.-E., "Cudamcml: User manual and implementation notes," (2009). http://www.lth.se/fileadmin/atomfysik/Biophotonics/Software/CUDAMCML.pdf.

[13] Maiti, R., Duan, M., Danby, S. G., Lewis, R., Matcher, S. J., and Carré, M. J., "Morphological parametric mapping of 21 skin sites throughout the body using optical coherence tomography," *Journal of the Mechanical Behavior of Biomedical Materials* **102**, 103501 (2020).

[14] Chopra, K., Calva, D., Sosin, M., Tadisina, K., Banda, A., Cruz, C. D. L., Chaudhry, M., Legesse, T., Drachenberg, C., Manson, P., and Christy, M., "A comprehensive examination of topographic thickness of skin in the human face," *Aesthet Surg J* **35**, 1007–13 (2015).

[15] Robertson, K. and Re, J. L., "Variation in epidermal morphology in human skin at different body sites as measured by reflectance confocal microscopy," *Medical Journals Limited* **90**, 368–373 (2010).

[16] Jacques, S. L., "Optical properties of biological tissues: a review," *Physics in Medicine and Biology* **58**, R37–R61 (may 2013).

[17] Meglinski, I. V. and Matcher, S. J., "Quantitative assessment of skin layers absorption and skin reflectance spectra simulation in the visible and near-infrared spectral regions," *Physiol. Meas* **23** (2002).

[18] Colas, V., Daul, C., Khairallah, G., Amouroux, M., and Blondel, W., "Spatially resolved diffuse reflectance and autofluorescence photon depth distribution in human skin spectroscopy: a modeling study," in [*Optics in Health Care and Biomedical Optics X*], Luo, Q., Li, X., Gu, Y., and Zhu, D., eds., **11553**, 82 – 96, International Society for Optics and Photonics, SPIE (2020).

[19] Krishnaswamy, A. and Baranoski, G. V. G., "Understanding penetration depth vs. wavelength for biosensor applications," (2004). Technical Report CS-2004-01.

[20] Prahl, S., "A compendium of tissue optical properties," (2020). http://omlc.ogi.edu/spectra/.

[21] Rakotomanga, P., *Inversion de modèle et séparation de signaux de spectroscopie optique pour la caractérisation in vivo de tissus cutanés*, PhD thesis, Université de Lorraine - Nancy (2019).

[22] Kazanci, H. O. and Canpolat, M., "Depth normalization algorithm for continuous wave reflectance diffuse optical tomography system," *El-Cezeri Journal Of Science And Engineering* **2**, 40–46 (01 2015).

[23] Stratonnikov, A. and Loschenov, V., "Evaluation of blood oxygen saturation in vivo from diffuse reflectance spectra," *Journal of Biomedical Optics* **6**, 457–67 (11 2001).